Desalination and Water Treatment
www.deswater.com
doi: 10.1080/19443994.2014.989274

57 (2016) 3846–3860
February

Taylor & Francis
Taylor & Francis Group

Theoretical and experimental studies of immediate assisted solar air gap membrane distillation systems

Chii-Dong Ho[a,*], Choon Aun Ng[b], Po-Hsiang Wang[a], Chun-Hsuan Cheng[a]

[a]*Department of Chemical and Materials Engineering, Tamkang University, New Taipei, Taiwan, Tel. +886 2 26215656; Fax: +886 2 26209887; emails: cdho@mail.tku.edu.tw (C.-D. Ho), mars380@hotmail.com (P.-H. Wang), 601400574@s01.tku.edu.tw (C.-H. Cheng)*
[b]*Department of Environmental Engineering, FEGT, UTAR, Kampar, Malaysia, email: ngca@utar.edu.my*

Received 14 May 2014; Accepted 11 November 2014

ABSTRACT

A new design of the air gap membrane distillation (AGMD) system equipped with a solar absorber was investigated theoretically and experimentally for saline water desalination, which integrated the immediate assisted solar (IAS) absorber as an additional heat supply source and the AGMD process to produce high purity water, say the IAS–AGMD system. The theoretical formulations were developed and the resultant equations were solved by the Newton–Raphson method. The theoretical predictions show that the IAS–AGMD system accomplishes a better device performance in pure water productivity than that of the conventional AGMD system. The good agreement was achieved between the theoretical predictions and the experimental runs in the present study. The effects of the fluid inlet temperature, volumetric flow rate, air gap thickness, and incident solar radiation on the heat transfer efficiency and pure water productivity were also delineated. The theoretical results indicate that the pure water productivity increases with increasing the inlet temperature of hot fluid, volumetric flow rate, and incident solar radiation but with decreasing the air gap thickness and inlet cold fluid temperature. Moreover, the theoretical prediction of the optimal process thermal efficiency in the IAS–AGMD system was obtained as the air gap thickness is 2.5 mm.

Keywords: Air gap membrane distillation; Solar collector; Saline water desalination; Pure water; Productivity improvement

1. Introduction

Potable water supplies are generally from lake or ground water with the water-shortage problem of the near future. Fortunately, seawater is an abundant resource and nearly inexhaustible storage that covers three quarters of the earth's surface if its high salinity could be removed by suitable separation processes. The desalination of dissolved salts has received a great deal of attention in the literature with applications and developments of membrane distillation (MD) systems [1–3]. It is natural to speculate on the applicability of MD to four configurations with the classification on the nature of the cold side of the membrane, i.e. direct contact (DCMD), air gap membrane distillation (AGMD), sweeping gas (SGMD), and vacuum (VMD). The advantages of MD systems lie in their simplicity

*Corresponding author.

and low operating cost by using low-grade thermal energy. The transport mechanism of the MD technology is a thermal-driven process to create a pressure gradient, in which only water vapor molecules are transported across porous hydrophobic membranes. Nearly 100% rejection of dissolved solids [4] provides high quality condensate resulting in the high purity water production.

There are several factors that affect the cost of pure water productivity such as plant capacity, qualified labor, energy cost, and amortization [5–7], and energy cost is the most concerned issue on some dominant devices for desalination with the alternative renewable energy source. The promising substitute for fossil fuels is solar energy to reduce environmental pollution and to immediately and easily equip MD systems, where energy demand is supplied entirely by flat-plate solar thermal collectors and photovoltaic cells. The application of solar energy has been developed by several investigators [8,9]. The solar driven MD desalination system has become economic and technically feasible strategies for drinking water production due to the advance of membrane materials and technology for last decades. The AGMD is best suited for applications where water vapor is the major permeate component [10–13]. The purpose of interposing an air gap in the AGMD systems between the membrane and condensation surface is to allow the water vapor diffusing through the air gap channel and in contact with the cooling plate. AGMD is one of the phase change desalination process and can be more economic by adding alternative energy sources, the most suitable solar energy, is considered cheap and accessible. Solar energy was collected with an absorber plate for preheating seawater to drive the phase change process in a smaller installation of membrane separation modules. A new design of immediate assisted solar air gap membrane distillation (IAS–AGMD) is a small-scale unit which combines the advantages of the traditional AGMD system and the thermally driven process with implementing solar absorbers onward the top surface as the heat source. The thermal-driven membrane separation process that involves transport of vapor through porous hydrophobic membranes may be employed to produce portable water in remote villages or rural areas with drinking water shortage. The potential for this process should be a technically feasible consideration with coupling a compound parabolic collector (CPC type) although the solar thermally driven MD process is relatively expensive when compared with other desalination processes. The promising cost advantages over rival desalination technologies may be exploited due to technological improvements and improvements in new membranes and module designs.

The solar radiation was collected with an absorber plate [14] for supplying the thermal energy required to preheat seawater and to result in a vapor pressure difference across the membrane owing to a temperature difference, and thus, the water vapor transports through the membrane with the water condensate collected on the cooling plate. Under laminar flow operation, the electricity requirements are lower than that in other conventional pressure-driven desalination processes [15]. The purposes of this study are to design an economic IAS–AGMD system when compared to the traditional AGMD system and to develop a mathematical model for predicting the pure water productivity of the IAS–AGMD system. The absorber plate and flow channel temperature distributions were obtained to investigate the pure water productivity and the effects of the operating parameters. The influences of inlet hot and cold fluid temperatures, volumetric flow rate, air gap thickness, and solar irradiation strength on the pure water productivity are also discussed.

2. Mathematical modeling of the IAS–AGMD conventional AGMD systems

For the IAS–AGMD and conventional AGMD systems, the heat transfer mechanisms take place in the domains including the hot feed, membrane, air gap, cooling plate, and the cold fluid of the distillation process are shown in Figs. 1(a) and 1(b), respectively. The vapor flux diffuses through the membrane and air gap prior to be cooled and collected. The tilted module used in the present study was set up at an angle of 27°C to the horizon for simulating IAS–AGMD device as referred to angle incident [16]. The theoretical analysis is based on the following assumptions: (a) physical properties of fluid, plates, and membrane are constants; (b) the condensate forms a thin liquid film and covers the entire condensing surface; (c) well insulation on the bottom and edge sides of modules; (d) under steady-state operations. The pure water productivity was estimated by solving the energy balance equations for (1) the hot feed stream, (2) hydrophobic membrane, (3) air gap, (4) cooling plate, (5) cooling water, (6) glass cover region, and (7) absorber plate region. These energy balance equations under steady-state operation for the convectional AGMD may be written as follows:

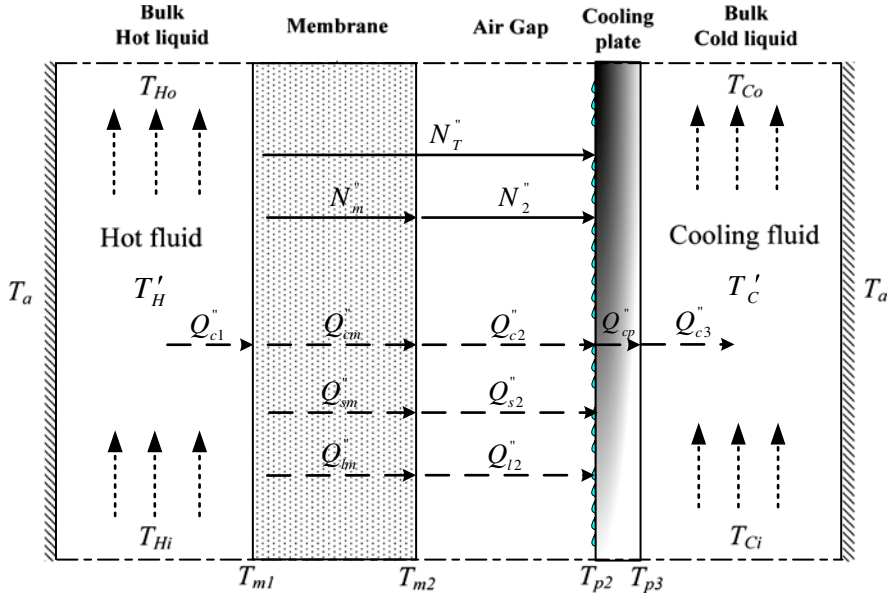

Fig. 1(a). Heat and mass transfers in the conventional AGMD module.

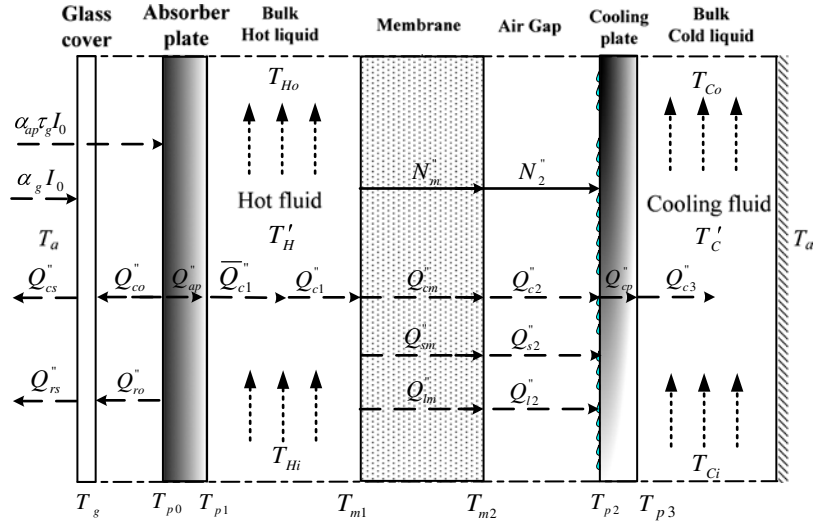

Fig. 1(b). Heat and mass transfers in the immediate assisted solar IAS–AGMD module.

2.1. The hot solution region

The net enthalpy flux entering to hot feed stream is equal to the heat flux transferring by convection

$$Q_{c1}'' = h_1(T_H' - T_{m1}) = \frac{\rho_H V_H Cp_H}{LW}\ (T_{Hi} - T_{Ho}) \tag{1}$$

or

$$h_1(T_H' - T_{m1}) + \frac{\rho_H V_H Cp_H}{LW}\ (T_{Ho} - T_{Hi}) = 0 \tag{2}$$

2.2. Energy flux from hot feed stream to membrane surface

The total enthalpy flux transferring to membrane surface is the sum of the heat conduction across the membrane, the enthalpy contents of the horizontal water vapor flow and the enthalpy of evaporation for water,

$$Q_{c1}'' = h_1(T_H' - T_{m1})$$

$$= Q''_{cm} + Q''_{sm} + Q''_{lm} = \left(\frac{k_m}{\delta_m} + N''_m Cp_v\right)(T_{m1} - T_{m2}) + N''_m \lambda \tag{3}$$

where $T'_H = \frac{T_{Hi}+T_{Ho}}{2}$ and $k_m = \varepsilon k_{air} + (1-\varepsilon)k_{solid}$, and then Eq. (3) can be rewritten to Eq. (4)

$$h_1\left[\frac{T_{Hi}+T_{Ho}}{2} - T_{m1}\right] - N''_m\lambda - \left[\frac{\varepsilon k_{air} + (1-\varepsilon)k_{solid}}{\delta_m} + N''_m Cp_v\right](T_{m1} - T_{m2}) = 0 \tag{4}$$

2.3. Energy flux from membrane through air gap domain to cooling plate surface

The energy flux transfers across the air gap in a similar way as described above. The total energy flux transferring to the cooling plate surface is the sum of both heat conduction and convection across the air gap between the temperatures at the interfaces of both sides of air gap, say membrane (T_{m2}) and air gap (T_{p2}), the enthalpy contents of the horizontal water vapor flow and the enthalpy of vapor.

$$Q'_{c1} = Q''_{c2} + Q''_{s2} + Q''_{12} = \left(U_2 + N''_2 Cp_v\right)\left(T_{m2} - T_{p2}\right) + N''_2\lambda \tag{5}$$

where $U_2 = h_2 + \frac{k_2}{\delta_2}$ and $k_2 = y_w k_v + (1-y_w)k_{air}$, and Eq. (5) can be rewritten to Eq. (6)

$$h_1(T'_{\mathrm{H}} - T_{m1}) - (U_2 + N''_2 Cp_v)\ (T_{m2} - T_{p2}) - N''_2\lambda = 0 \tag{6}$$

2.4. Energy flux transferring through the cooling plate

As the vapor flux reaches the condensation surface, it condenses and forms a condensate film. The condensate film thickness was estimated to be 8.5×10^{-5} m [13], and thus, the thermal resistance in the condensate film domain during this model derivation can be neglected. Meanwhile, pure water productivity is small in the present work, and no flooding of water and the condensate film covering entire condensation surface were assumed. When the energy flux reaches the condensation surface, the enthalpy content of the condensed water was transported downward to the cooling plate, the enthalpy of evaporation could be transported by heat conduction from the condensation surface to the cold feed stream with the temperatures at the interfaces of both sides on the cooling plate, say T_{p2} and T_{p3}

$$Q''_{cp} = \frac{k_p}{\delta_p}\left(T_{p2} - T_{p3}\right) \tag{7}$$

2.5. Energy flux from condensation layer to cold feed stream

The amount of energy transfer from the cooling plate to the cold feed stream is described as

$$Q''_{c3} = h_3\left(T_{p3} - T'_C\right) \tag{8}$$

Eq. (8) can be rewritten if the equivalent thermal resistance with the temperature difference $(T_{p2} - T'_C)$ was used

$$Q''_{c3} = \left(\frac{\delta_p}{k_p} + \frac{1}{h_3}\right)^{-1}(T_{p2} - T'_C) \tag{9}$$

2.6. The cold feed region

The energy flux entering to cold feed stream is equal to the energy flux transferring by convection to the flowing fluid

$$Q''_{c3} = \frac{\rho_C V_C Cp_C}{LW}(T_{Co} - T_{Ci}) \tag{10}$$

In addition, there are two more energy balance equations for describing the energy flux in IAS–AGMD systems were needed due to the IAS–AGMD device by adopting the widespread flat plate collector (FPC) as the heat supply source. The FPC has a coated absorber plate with the open duct for transporting heated saline water, a glass pane covered on the top, and insulation on the sides and the bottom. The mass and energy fluxes for all layers are illustrated in Fig. 1(b) with adding the heat transfer rate by convection from the absorber plate $\bar{Q}''_{c1}$ as follows:

2.7. The glass cover

$$\alpha_g I_0 + Q''_{c0} + Q''_{r0} = Q''_{ca} + Q''_{ra} \tag{11}$$

in which

$$Q''_{c0} = h_0(T_{p0} - T_g), Q''_{r0} = \frac{\sigma\left(T_{p0}^4 - T_g^4\right)}{1/e_p + 1/e_g - 1},$$
$$Q''_{ca} = h_a(T_g - T_a), \quad Q_{ra} = e_g\sigma({T_g}^4 - {T_a}^4),$$
$$F_{pg} = \frac{1}{1/e_p + 1/e_g - 1} \tag{12}$$

Substitutions of all definitions in Eq. (12) into Eq. (11) yields

$$T_g = \frac{\alpha_g I_0 + h_0 T_{p0} + h_a T_a + F_{pg}\sigma(T_{p0}^4 - T_g^4) - \sigma e_g(T_g^4 - T_a^4)}{h_0 + h_a} \tag{13}$$

2.8. The absorber plate

Thermal energy flux was provided to heat the flowing fluid according to a given solar incident radiation, and the energy balance equation for the absorber plate as

$$\alpha_{ap}\tau_g I_0 = Q''_{co} + Q''_{ro} + Q''_{ap} \tag{14}$$

$$Q''_{ap} = \frac{k_p}{\delta_p}(T_{p0} - T_{p1})$$

$$= h_1(T_{p1} - T'_H) = \bar{Q}''_{c1} \tag{15}$$

Eq. (15) can be rewritten if the equivalent thermal resistance with the temperature difference $(T_{p0} - T_H)$ was used

$$Q''_{ap} = \left(\frac{\delta_p}{k_p} + \frac{1}{h_1}\right)^{-1}(T_{p0} - T'_H) \tag{16}$$

Substitutions of Eqs. (12) and (16) into Eq. (14) gives

$$T_{p0} = \frac{\alpha_p\tau_g I_0 + \left(\frac{h_1 k_p}{k_p + h_1\delta_p}\right)T'_H + h_0 T_g - F_{pg}\sigma(T_{p0}^4 - T_g^4)}{h_1 + h_0} \tag{17}$$

Combination of Eqs. (9) and (10) gives the energy flux to the cold feed stream, i.e.

$$Q''_{c3} = \left(\frac{\delta_p}{k_p} + \frac{1}{h_3}\right)^{-1}(T_{p2} - T_C) = \frac{\rho_C V_C Cp_C}{BL}(T_{Co} - T_{Ci}) \tag{18}$$

or

$$Q''_{c3} = \left(\frac{\delta_p}{k_p} + \frac{1}{h_3}\right)^{-1}\left(T_{p2} - \frac{T_{Ci} + T_{Co}}{2}\right)$$
$$= \frac{\rho_C V_C Cp_C}{BL}(T_{Co} - T_{Ci}) \tag{19}$$

where $T'_C = (T_{Ci} + T_{Co})/2$. The outlet temperature of the cold stream is thus obtained as

$$T_{Co} = \frac{2\frac{h_3 k_p}{h_3\delta_p + k_p}T_{p2} + \left(2\frac{\rho_C V_C Cp_C}{LW} - \frac{h_3 k_p}{h_3\delta_p + k_p}\right)T_{Ci}}{2\frac{\rho_C V_C Cp_C}{LW} + \frac{h_3 k_p}{h_3\delta_p + k_p}} \tag{20}$$

Similarly, the equivalent thermal resistance in terms of the temperature difference $(T_{p2} - T_{Ci})$ was used to express the energy flux from the cooling plate to cooling fluid including all thermal resistances as follows:

$$Q''_{c3} = \left(\frac{\delta_p}{k_p} + \frac{1}{h_3} + \frac{WL}{2\rho_C V_C Cp_C}\right)^{-1}(T_{p2} - T_{Ci}) \tag{21}$$

Since the heat transfer rate from the hot feed stream to cold fluid of the distillation process is constant throughout in all transferring layers, as seen in both Figs. 1(a) and 1(b), it follows that $Q''_{c1} = Q''_{c3}$

$$h_1(T' - T_{m1}) = \left(\frac{\delta_p}{k_p} + \frac{1}{h_3} + \frac{WL}{2\rho_C V_C Cp_C}\right)^{-1}(T_{p2} - T_{Ci}) \tag{22}$$

The heat transfer coefficients were estimated in correlated equation using for the Nusselt number [17] if the channel surface is smooth and under the laminar flow

$$Nu = 4.36 + \frac{0.036\ \mathrm{Re}\,\mathrm{Pr}\left(\frac{D_e}{L}\right)}{1 + 0.011\left[\mathrm{Re}\,\mathrm{Pr}\left(\frac{D_e}{L}\right)\right]^{0.8}} \tag{23}$$

However, the correlated equation for titled surface was investigated by Ayyaswamy and Catton [18] with existing in finding a boundary layer regime from $\phi = 0^\circ$ to $\phi = 90^\circ$ and Raleigh number Ra is high

enough, and the convective contribution to the heat transfer should follow the simple scaling law [19]

$$Nu_2 = \frac{h_2\delta_2}{k_2} = 1 + \left[0.197\left(\frac{L}{\delta_2}\right)^{-1/9} Ra_2^{1/4} - 1\right]\sin\phi \quad (24)$$

where Ra_2 is defined as [20]

$$Ra_2 = \frac{g\delta_2^3\beta_2}{\nu_2\alpha_2}\left[(T_{m2} - T_{p2}) + \frac{P_{m2}^{sat} - P_{p2}^{sat}}{2.65P_T - P_{m2}^{sat}}T_{m2}\right] \quad (25)$$

Moreover, there are two more heat transfer coefficients required for operating the IAS–AGMD system, say h_0 in the air layer and h_a for the ambient air. Hollands et al. [21] obtained an empirical expression for the heat transfer coefficient in free convection of an inclined air layer heated from below as

$$Nu_0 = \frac{h_0\delta_0}{k_0} = 1 + 1.44\left[1 - \frac{1,708}{Ra_0\cos\phi}\right]^+\left(1 - \frac{1,708\sin(1.8\phi)^{1.6}}{Ra_0\cos\phi}\right) + \left[\left(\frac{Ra_0\cos\phi}{5,830}\right)^{\frac{1}{3}} - 1\right]^+ \quad (26)$$

in which $Ra_0 = \frac{g\delta_0^3\beta_0\Delta T}{\nu_0\alpha_0} = \frac{g\delta_0^3\beta_0(T_{p0} - T_g)}{\nu_0\alpha_0}$ and $[\,]^+ = \frac{(|x| + x)}{2}$.

The convective heat-transfer coefficient for air flowing over the glass cover may be calculated using the following empirical equation [22]

$$h_a = 4.8 + 3.3V \quad (27)$$

2.9. The solution procedure

There are four unknown temperatures, the temperature on the both sides of membrane surfaces (T_{m1} and T_{m2}), temperature on the cooling plate (T_{p2}), and outlet temperature of the hot stream (T_{Ho}), were determined by solving Eqs. (2), (4), (6), and (22) numerically with the use of Newton–Rophson method, as indicated in Fig. 2. The Newton–Raphson method is a powerful technique for solving non-linear algebraic equations known on roots finding with devastating efficiency. The outlet cold stream temperature (T_{Co}) was thus checked by Eq. (20) once the above four temperatures were obtained. Prediction of the improvement of the convectional AGMD device performance is to calculate the water permeate flux from the hydrophobic membrane. The mass transfer driving force

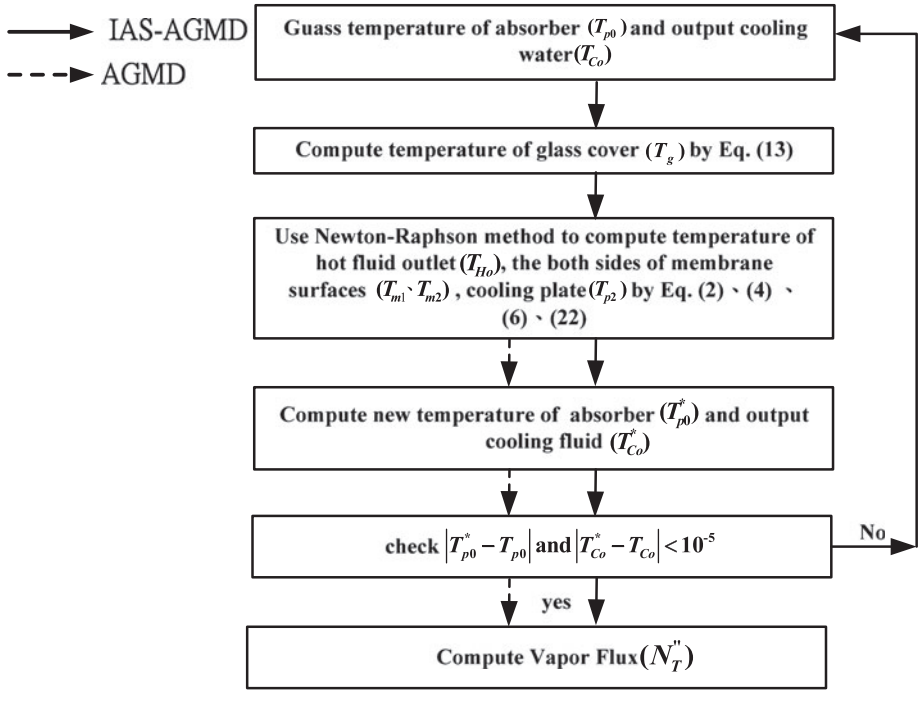

Fig. 2. Flow diagram of the algorithm for prediction of the vapor flux.

across the membrane is the difference in saturated pressure components on both membrane surfaces as a response to the temperature gradient, and hence, the vapor flux diffusing to the cooling plate as the collected water condensate. The following equation can be used to express the amount of vapor flux that passes through the membrane pores:

$$N''_m = C_m \Delta P = C_m (P_1^{sat} - P_{m2}^{sat}) \tag{28}$$

where P_{m1}^{sat} and P_{m2}^{sat} are the saturated pressure of water vapor on the membrane surfaces in hot feed stream and on the air gap layer. For non-ideal binary mixtures, the partial pressure can be determined as

$$P_1^{sat} = y_w\, p = x_w\, a_w\, P_{m1}^{sat} \tag{29}$$

where y_w and x_w are the vapor and liquid mole fractions of water, respectively, and P and P_{m1}^{sat} are the total pressure and saturation pressure of pure water, respectively. The water activity in NaCl solutions a_w is a function of the temperature and composition determined [1]. For the NaCl solution, the effect of lowered water saturation vapor pressure by the non-volatile solute can be accounted for using the correlated expression for water activity coefficient (a_w):

$$a_w = 1 - 0.5x_{\mathrm{NaCl}} - 10x_{\mathrm{NaCl}}^2 \tag{30}$$

The equation of the membrane permeation coefficient is reported to be applicable for deaerated microporous membranes [23] with the dominant mass transfer mechanism of Knudsen diffusion and molecular diffusion by using a semi-empirical equation as follows:

$$C_m = \left(\frac{1}{C_{km}} + \frac{1}{C_{Mm}}\right)^{-1} = \left\{ \left[1.064 \frac{\varepsilon r_p}{\tau \delta_m} \left(\frac{M_w}{R\bar{T}_m}\right)^{1/2}\right]^{-1} + \left[\frac{1}{Y_{\ln}} \frac{D_m \varepsilon}{\tau \delta_m} \frac{M_w}{R\bar{T}_m}\right]^{-1} \right\}^{-1} \tag{31}$$

where the tortuosity τ of the porous hydrophobic, say PTFE, was estimated [24]

$$\tau = \frac{1}{\varepsilon} \tag{32}$$

Moreover, the equation that expresses the molar vapor diffusion flux in terms of the saturated pressure of water vapor on both sides of the air gap layer when it diffuses through a stagnant air film

$$N''_2 = C_2 (P_{m2}^{sat} - P_{p2}^{sat}) \tag{33}$$

in which the diffusion coefficient is [25]

$$C_2 = C_{M2} = \left(\frac{1}{Y_{\ln}} \frac{D_2}{\delta_2} \frac{M_w}{R\bar{T}_2}\right) \tag{34}$$

Combination of Eqs. (28) and (33) gives

$$N''_m = N''_2 = N''_T = C_T (x_{water}\, a_{water}\, P_{m1}^{sat} - P_{p2}^{sat}) \tag{35}$$

where

$$C_T = \left(\frac{1}{C_m} + \frac{1}{C_2}\right)^{-1} = \left(\frac{1}{C_{km}} + \frac{1}{C_{Mm}} + \frac{1}{C_{M2}}\right)^{-1} = \left\{ \left[1.064 \frac{\varepsilon r_p}{\tau \delta_m} \left(\frac{M_w}{R\bar{T}_m}\right)^{1/2}\right]^{-1} + \left[\frac{1}{Y_{\ln}} \frac{D_m \varepsilon}{\tau \delta_m} \frac{M_w}{R\bar{T}_m}\right]^{-1} + \left[\left(+\frac{1}{Y_{\ln}} \frac{D_2}{\delta_2} \frac{M_w}{R\bar{T}_2}\right)^{-1}\right] \right\}^{-1} \tag{36}$$

3. Experimental apparatus and setup

The integrated MD setups for the IAS–AGMD and conventional devices are illustrated in Figs. 3(a) and 3(b), respectively. The IAS–AGMD and conventional AGMD devices are 0.25 m in effective width and 0.20 m in effective length with 0.002 m thickness in channel height, and distance among glass cover and absorber plate is 0.01 m of IAS–AGMD module. The IAS–AGMD module was constructed including glass cover, acrylic plate, blackened absorber plate, flexible silicon frame as the fluid spacer, composite membrane PTFE, and cooling plate, and then combined together with screws and nuts, as indicated in Fig. 4(a) while the AGMD module without the glass cover, acrylic plate, blackened absorber plate are shown in Fig. 4(b). The spacers are made of silicon dioxide (silicon gel) to create channels for fluid flowing. The wound grid of nylon fibers with 1.4×10^{-4} m of diameter inserted between the spacer and membrane surface to prevent from membrane bending and wrinkling in the hot stream channel while the galvanized gridiron was implemented as a support between the spacer and membrane surface in the air gap channel, as shown in Figs. 4(a) and 4(b), respectively. The acrylic plate has

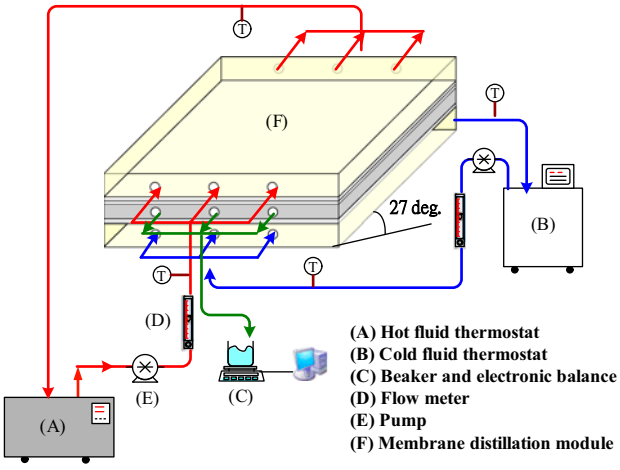

Fig. 3(a). Experimental setup of the conventional AGMD system.

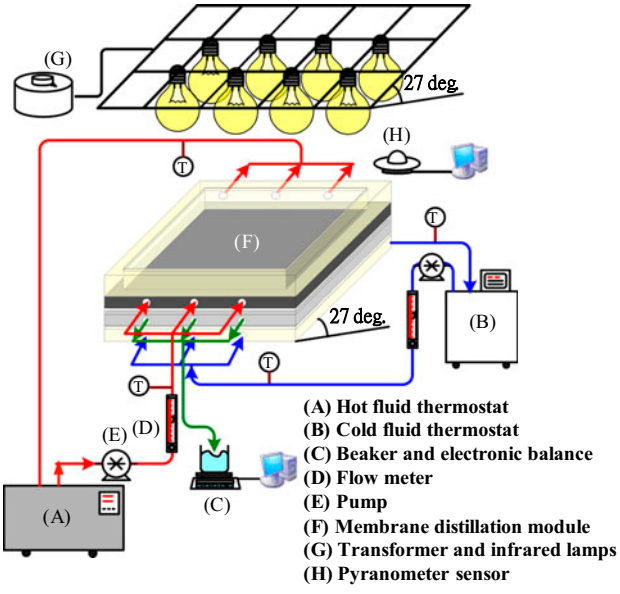

Fig. 3(b). Experimental setup of the IAS–AGMD system.

three distribution holes for the fluid flowing in and out at both entrance and exit ends, respectively. The experimental equipment for IAS–AGMD was carried out with an artificial simulator consisting of 8 lamps by a transformer to adjust irradiance intensity. The incident solar radiation I_0 was measured with an Epply laboratory pyranometer. The saline water flows into both the IAS–AGMD and conventional AGMD modules with the same inlet temperature for comparisons except for the saline water being heated under the absorber plate in operating the IAS–AGMD system. In all experimental runs, the IAS–AGMD and conventional AGMD systems were inclined at an angle of 27° and well insulated except for the glass cover to prevent the heat loss to the environment. The hot feed fluid is an aqueous solution of 3.5 wt% sodium chloride and the cold fluid is the pure water, and the permeate flux was overflowed and measured by using an electronic balance. Under the given operating conditions, the overflowed pure water was collected and weighed using an electronic balance at 10 min intervals until steady state was reached as indicated by no change in weighing the produced pure water. The results were compared with the mathematical models in this paper. The pure water productivity using the IAS–AGMD module is enhanced by 2.6–13.4% when compared to the conventional AGMD module for implementing the IAS absorber due to increasing the inlet saline water

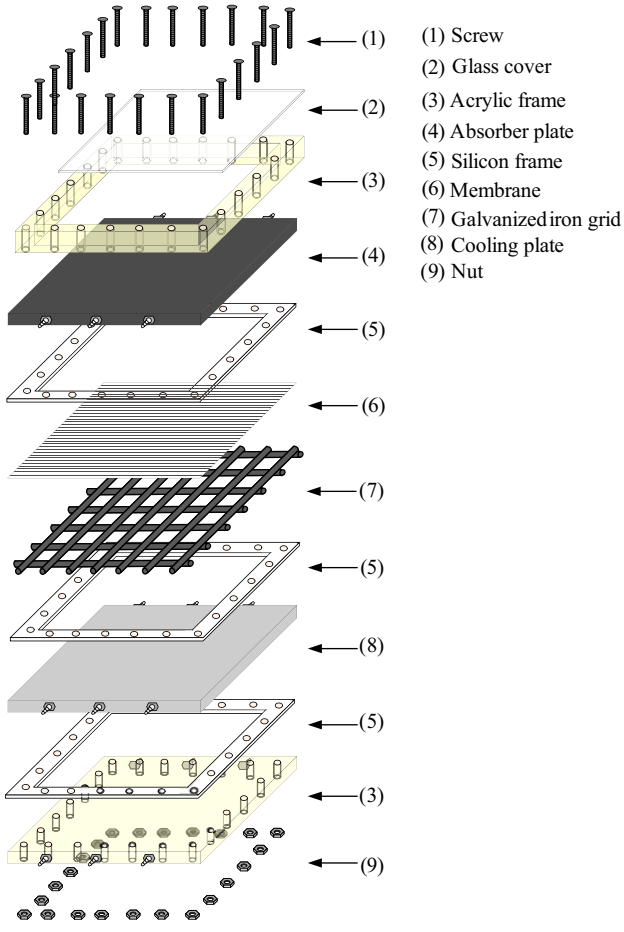

Fig. 4(a). Isometric view of the IAS–AGMD module on its sides.

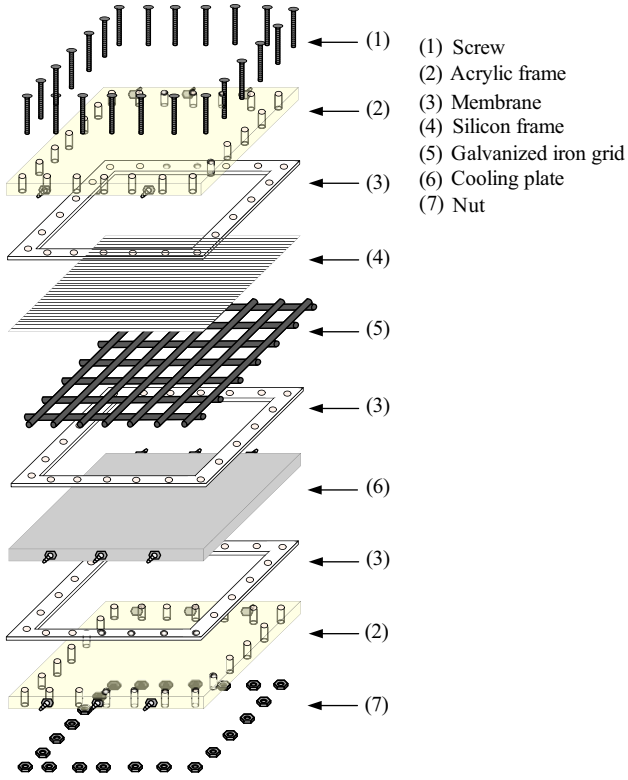

Fig. 4(b). Isometric view of the AGMD module on its sides.

temperature, as indicated in Tables 1–4. The experimental runs were conducted for various inlet hot fluid temperatures (313, 318, 323, 328 K), inlet cold fluid temperatures (288, 293, 298 K), and flow rate variations (0.3, 0.5, 0.7, 0.9 L/min) and monitored continually. The flow rates of both hot and cold fluids were kept the same.

4. Results and discussion

The influences of the main parameters on vapor flux N''_T for both conventional AGMD and IAS IAS–AGMD are analyzed. These include the inlet hot fluid temperature, inlet cold fluid temperature, flow rate, solar radiation intensity, and air gap thickness. The differences between the theoretical predictions and the experimental results are less than 10%. The results of vapor flux with varying the air gap thickness, the inlet hot fluid temperature, and with or without the solar intensity are shown in Table 1 while the vapor fluxes with the inlet cold fluid temperature as a parameter are shown in Table 2. The vapor flux productivity increases with increasing the hot fluid inlet temperature, therefore, a relative smaller amount of vapor flux was produced in IAS–AGMD systems operated at lower hot fluid inlet temperatures, and thus, a larger relative error is calculated by Eq. (37) in Table 1. Restated, a slight increment of the vapor flux with decreasing of the inlet cold fluid temperature was observed due to the increase in the partial pressure gradient, as referred to the driving force, and hence, the vapor flux of AGMD device is not very sensitive to the inlet cold fluid temperature, as indicated in Table 2. This negligible influence can be attributed to the low water vapor pressure, which is obtained from Antoine equation at lower temperatures, and results in little benefit due to the small driving force increment of the hot and cold sides. The air gap thickness and inlet hot fluid temperature are the most important factors affecting AGMD device performance, as indicated from Tables 1 and 2. The vapor flux increases with increasing the inlet hot fluid temperature, but with decreasing the air gap thickness and inlet cold fluid temperature.

Table 1
Comparisons of simulation and experimental results for AGMD and IAS–AGMD of different thickness of the air gap, T_{Ci} = 298 K, $V_C = V_H$ = 0.9 L/min

		AGMD			IAS–AGMD (I_0 = 830 W/m^2)		
Air gap (mm)	T_{Hi} (K)	$N''_{theo.}$ (kg/m^2 h)	$N''_{exp.}$ (kg/m^2 h)	Error (%)	$N''_{theo.}$ (kg/m^2 h)	$N''_{exp.}$ (kg/m^2 h)	Error (%)
2	308	0.593	0.558	6.27	0.631	0.577	9.36
	318	1.496	1.453	2.96	1.552	1.595	2.70
	328	2.742	2.687	2.05	2.819	2.837	0.63
4	308	0.338	0.322	4.97	0.360	0.333	8.11
	318	0.879	0.799	10.01	0.914	0.882	3.63
	328	1.678	1.710	1.87	1.729	1.731	0.12
10	308	0.151	0.149	1.34	0.161	0.152	5.92
	318	0.404	0.399	1.25	0.421	0.420	0.24
	328	0.801	0.858	6.64	0.827	0.864	4.28

Table 2
Comparisons of simulation and experimental results for AGMD and IAS–AGMD of different cold fluid inlet temperature and fluid flow rate, T_{Hi} = 323 K, V_H = 0.9 L/min

			AGMD			IAS–AGMD (I_0 = 830 W/m^2)		
Air gap (mm)	T_{Ci} (K)	V_C (L/min)	$N''_{theo.}$ (kg/m^2 h)	$N''_{exp.}$ (kg/m^2 h)	Error (%)	$N''_{theo.}$ (kg/m^2 h)	$N''_{exp.}$ (kg/m^2 h)	Error (%)
2	298	0.3	1.996	1.974	1.11	2.059	2.126	3.15
		0.5	2.040	2.051	0.54	2.105	2.181	3.48
		0.7	2.061	2.061	0	2.127	2.203	3.45
		0.9	2.074	2.142	3.17	2.140	2.313	7.48
	293	0.3	2.207	2.329	5.24	2.271	2.551	10.98
		0.5	2.246	2.355	4.63	2.311	2.563	9.83
		0.7	2.264	2.366	4.31	2.329	2.567	9.27
		0.9	2.275	2.376	4.25	2.341	2.573	9.02
	288	0.3	2.369	2.438	2.83	2.433	2.609	6.75
		0.5	2.401	2.498	3.88	2.466	2.653	7.05
		0.7	2.416	2.582	6.43	2.480	2.703	8.25
		0.9	2.424	2.606	6.98	2.489	2.706	8.02
4	298	0.3	1.216	1.143	6.39	1.258	1.315	4.33
		0.5	1.231	1.183	4.06	1.273	1.360	6.40
		0.7	1.238	1.223	1.23	1.281	1.368	6.36
		0.9	1.243	1.264	1.66	1.285	1.397	8.02
	293	0.3	1.332	1.333	0.08	1.373	1.468	6.47
		0.5	1.344	1.358	1.03	1.386	1.545	10.29
		0.7	1.350	1.366	1.17	1.392	1.546	9.96
		0.9	1.354	1.381	1.96	1.396	1.566	10.86
	288	0.3	1.418	1.462	3.01	1.459	1.556	6.23
		0.5	1.428	1.470	2.86	1.470	1.610	8.70
		0.7	1.433	1.481	3.24	1.474	1.662	11.31
		0.9	1.435	1.504	4.59	1.477	1.664	11.24

The accuracy of the theoretical predictions of vapor flux by measuring the deviation from the experimental results was estimated using the following definition as

$$E = \frac{1}{n_{exp}} \sum_{i=1}^{N_{exp}} \frac{|\eta_{theo,i} - \eta_{exp,i}|}{\eta_{theo,i}} \times 100\% \quad (37)$$

where $n_{exp,i}$, $N''_{theo,i}$ and $N''_{exp,i}$ are the number of experimental runs, theoretical prediction, and experimental results of vapor fluxes, respectively. The accuracy deviations are shown in Tables 3 and 4 for both AGMD and IAS–AGMD configurations, respectively. The agreement between the experimental results and theoretical predictions is fairly good with the error analysis of $0 \le E \le 17.11$ and $0.53 \le E \le 10.96$ for various hot fluid inlet temperature and various solar radiation, respectively, as shown in Figs. 5 and 6. Although the deviation is relatively high for some experimental runs, a qualitative agreement pertaining to the trend of vapor flux productivity is achieved. The largest deviation occurs at the lower hot fluid inlet temperature of AGMD systems since a relative smaller amount of vapor flux was produced in AGMD systems operating at lower hot fluid inlet temperatures, and thus, a larger relative error is calculated by Eq. (37) in Table 3.

The experimental results show that the vapor flux increases with increasing the hot feed flow rate to be explained by the temperature polarization phenomenon, as confirmed in Table 3 and Figs. 5(a) and 5(b) for both conventional and immediate assisted soar AGMD processes. The operable condition to reduce the temperature and concentration polarization effects in AGMD process is aiming to increase the hot feed flow rate for establishing an adequate hydrodynamic condition under turbulent flow regime. Consequently, the boundary layer thickness reduction comes up with a driving force increment of vapor pressure difference and a higher vapor flux through the hydrophobic membrane. Moreover, the amount of the vapor flux is more sensitive to V_H because the heat transfer

Table 3
Comparisons of simulation and experimental results for AGMD and IAS–AGMD of different hot fluid inlet temperature and fluid flow rate, T_{Ci} = 298 K, V_C = 0.9 L/min

		Air gap = 4 (mm)					
		AGMD			IAS–AGMD (I_0 = 830 W/m^2)		
T_{Hi} (K)	V_H (L/min)	$N''_{theo.}$ (kg/m^2 h)	$N''_{exp.}$ (kg/m^2 h)	Error (%)	$N''_{theo.}$ (kg/m^2 h)	$N''_{exp.}$ (kg/m^2 h)	Error (%)
313	0.3	0.534	0.456	17.11	0.610	0.606	0.66
	0.5	0.560	0.487	14.99	0.609	0.556	9.53
	0.7	0.573	0.492	16.46	0.608	0.560	8.57
	0.9	0.580	0.496	16.94	0.608	0.531	14.50
318	0.3	0.796	0.738	7.86	0.887	0.868	2.19
	0.5	0.843	0.797	5.77	0.902	0.914	1.31
	0.7	0.865	0.798	8.40	0.909	0.919	1.09
	0.9	0.879	0.799	10.01	0.914	0.922	0.87
323	0.3	1.104	1.206	8.46	1.212	1.275	4.94
	0.5	1.181	1.231	4.06	1.252	1.279	2.11
	0.7	1.219	1.241	1.77	1.272	1.306	2.60
	0.9	1.243	1.264	1.66	1.285	1.397	8.02
328	0.3	1.461	1.496	2.34	1.585	1.602	1.06
	0.5	1.580	1.606	1.62	1.664	1.664	0.0
	0.7	1.641	1.665	1.44	1.704	1.695	0.53
	0.9	1.678	1.710	1.87	1.729	1.731	0.12

Table 4
Comparisons of simulation and experimental results for AGMD and IAS–AGMD of different intensity of solar radiation, T_{Hi} = 323 K, T_{Ci} = 298 K, V_C = 0.9 L/min

I_0 (W/m^2)	Air gap (mm)	V_H (L/min)	$N''_{theo.}$ (kg/m^2 h)	$N''_{exp.}$ (kg/m^2 h)	Error (%)
830	2	0.3	1.894	1.871	1.23
		0.5	2.026	1.950	3.90
		0.7	2.096	2.022	3.66
		0.9	2.140	2.026	5.63
	4	0.3	1.212	1.275	4.94
		0.5	1.252	1.279	2.11
		0.7	1.272	1.306	2.60
		0.9	1.285	1.397	8.02
1,100	2	0.3	1.950	2.075	6.02
		0.5	2.065	2.076	0.53
		0.7	2.125	2.051	3.61
		0.9	2.164	2.073	4.39
	4	0.3	1.252	1.366	8.35
		0.5	1.278	1.387	7.86
		0.7	1.292	1.424	9.27
		0.9	1.300	1.460	10.96
AGMD	4	0.3	1.104	1.206	8.46
		0.5	1.181	1.231	4.06
		0.7	1.219	1.241	1.77
		0.9	1.243	1.264	1.66

resistance of the hot stream in AGMD system is the dominant factor in affecting the total heat transfer rate. The validations of both models were made by comparing the theoretical predictions with the experimental results. The error analysis between the model predictions and the experimental results are less than

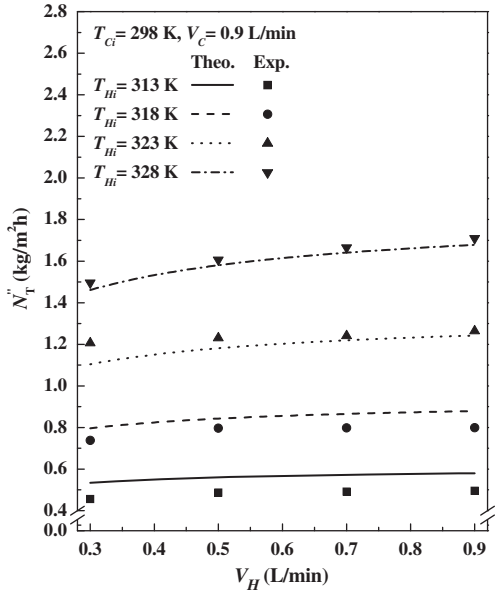

Fig. 5(a). Effects of hot fluid inlet temperature and fluid flow rate on the vapor flux for the AGMD system.

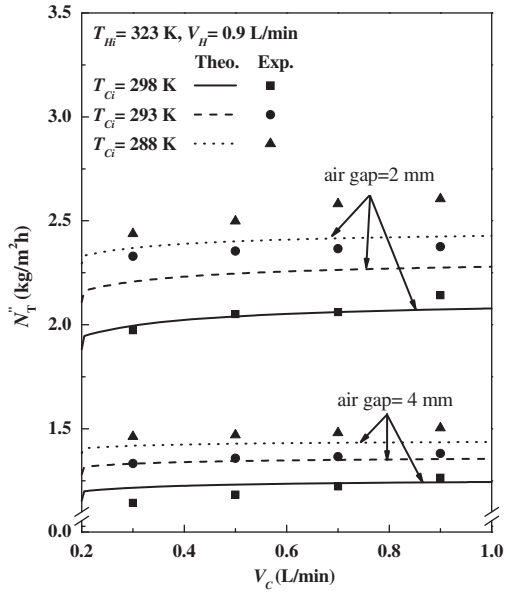

Fig. 6(a). Effects of cold fluid inlet temperature and fluid flow rate on the vapor flux of the AGMD system.

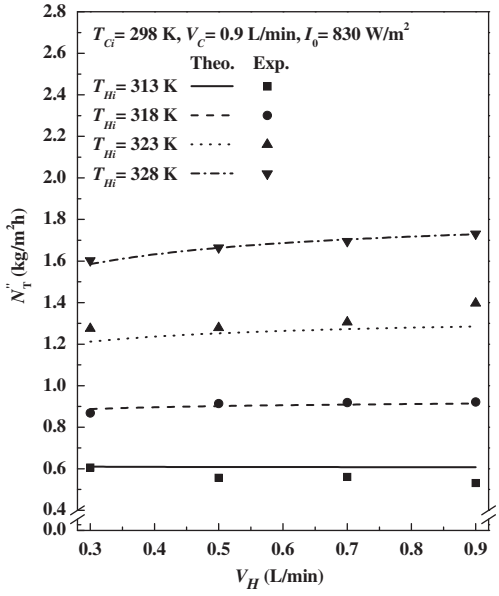

Fig. 5(b). Effects of hot fluid inlet temperature and fluid flow rate on the vapor flux of the IAS–AGMD system.

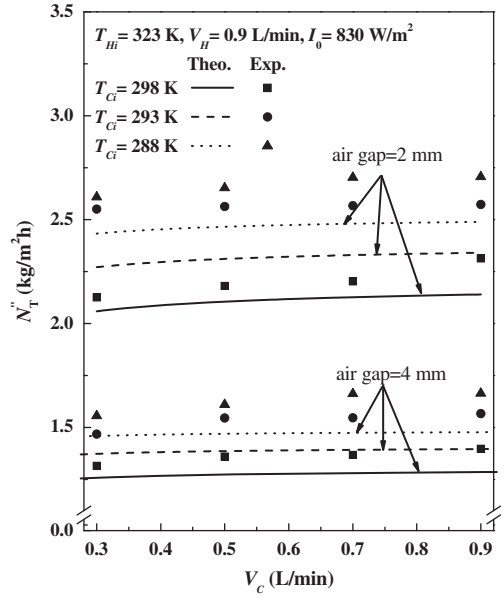

Fig. 6(b). Effects of cold fluid inlet temperature and fluid flow rate on the vapor flux of the IAS–AGMD system.

10%. The results of variations of the air gap thickness, solar intensity, and the flow rate of hot fluid are also shown in Figs. 6(a) and 6(b) and Table 4. Both theoretical and experimental results show that the vapor flux increases with increasing the solar intensity but with decreasing the air gap thickness. Meanwhile, the IAS–AGMD system attained a higher vapor flux of maximum value 13.4% than the conventional AGMD system under the same operating conditions. The suitable selections of the design parameter of air gap thickness (δ_2) and operating parameter of intensity of solar radiation I_0 on the process thermal efficiency in air gap channel are presented in Fig. 7. The process thermal efficiency in air gap channel can be defined as

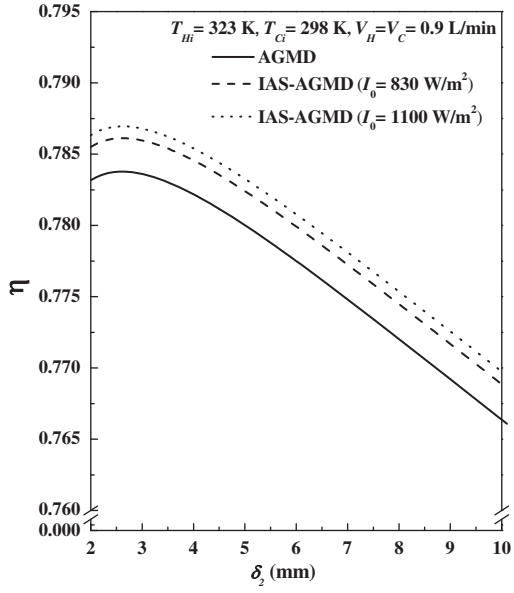

Fig. 7. The effect of the air gap thickness on process thermal efficiency for both AGMD and IAS–AGMD systems.

ratio of the heat transfer due to production of the distillate and the total heat transfer across the membrane, that is

$$\eta = \frac{N_2'' \lambda}{N_2'' \lambda + (U_2 + N_2'' C p_v)\ (T_{m2} - T_{p2})} \tag{38}$$

It is seen from Fig. 7 that the process thermal efficiency decreases with increasing the air gap thickness. The theoretical prediction of the optimal thermal efficiency in both AGMD and IAS–AGMD systems was obtained as the air gap thickness of 2.5 mm.

5. Conclusions

The new design of IAS–AGMD module for desalination has been investigated by both experimental and theoretical approaches. The IAS–AGMD system characteristics were implemented for both fluid heating and pure water production. The mathematical treatments, which is developed by considering both the heat and mass transfer of each layer of the module and verified by experimental data, provides a convenient tool for analysis of the IAS–AGMD module. Experimental study has demonstrated its feasibility and up to 13.4% of pure water production enhancement was obtained by the innovative IAS–AGMD system. The hot fluid inlet temperature and the air gap thickness are two significant parameters to affect the vapor flux in the air gap membrane desalination system. Further study in the present work shows that the IAS–AGMD with inserting solar absorber can obtain a greater enhancement in water production due to the assisted solar incident. The module scale and water production capability of IAS–AGMD system with IAS MD applications received a great attraction in having potential for drinking water production. Although the solar thermally driven MD process is relatively expensive when compared with other desalination processes, the design of thermal-driven membrane separation processes may be applied to produce portable water in remote villages or rural areas with drinking water difficulties. The module size and water productivity capability of IAS–AGMD system have the potential for the present process to be a technically feasible consideration with coupling a more energy-efficient CPC type of reflecting to the absorber all of the incident radiation within wide limits. Thermal efficiency and salt rejection are significant factors to be improved in designing this IAS–AGMD membrane technology to seawater desalination, and the prototype has been developed and manufactured by the Swedish company Scarab AB [26].

Acknowledgment

The authors thank the Ministry of Science and Technology of the Republic of China and Tamkang University for their financial support.

Nomenclature

a_w	—	water activity in NaCl solution
Cp	—	heat capacity (J/(kg K))
C_m	—	membrane transfer coefficient of membrane (kg/(m^2 Pa s)
C_a	—	membrane transfer coefficient of air gap (kg/(m^2 Pa s)
C_K	—	membrane transfer coefficient based on the Knudsen diffusion model (kg/(m^2 Pa s)
C_M	—	membrane transfer coefficient based on the molecular coefficient (kg/(m^2 Pa s)
D	—	diffusion coefficient (m^2/s)
D_e	—	hydraulic diameter (m)
E	—	deviation of the experimental runs from theoretical predictions, defined in Eq. (37)
g	—	gravitational acceleration (m/s^2)
h	—	heat transfer coefficient (W/(m^2 K))
k	—	thermal conductivity coefficient (W/m K)
L	—	conduit length (m)
I_0	—	intensity of solar radiation (W/m^2)
M_W	—	molecular weight (kg/mol)
N''	—	vapor flux (kg/(m^2·h)
n_{exp}	—	the number of the experimental runs

Nu — Nusselt number
Ra — Rayleigh number
Re — Reynolds number
Pr — Prandtl number
P^{sat} — saturated pressure (Pa)
P_T — total pressure (Pa)
P_m^{sat} — saturated pressure in membrane (Pa)
P_p^{sat} — saturated pressure on plate (Pa)
Q'' — heat flux (W/m^2)
Q''_{ap} — heat flux of absorber plate (W/m^2)
Q''_{cp} — heat flux of cooling plate (W/m^2)
Q''_c — conduction or convention heat flux (W/m^2)
Q''_s — sensible heat flux (W/m^2)
Q''_l — latent heat flux (W/m^2)
Q''_r — Radiation heat flux (W/m^2)
r_p — membrane pore radius (m)
R — gas constant (J/mol K)
T_a — temperature of atmosphere (K)
T_g — temperature of glass cover (K)
T_m — temperature of membrane (K)
T_p — temperature of plate (K)
T_C — temperature of cold stream (K)
T_H — temperature of hot stream (K)
$\bar{T}_2$ — average temperature of air gap (K)
U_2 — overall heat transfer coefficient of air gap ($W/(m^2\ K)$
V — volumetric flow rate of both hot and cold feed streams (m^3/s)
W — conduit width (m)
x_w — liquid mole fraction of water
x_{NaCl} — liquid mole fraction of NaCl
y_w — vapor mole fractions of water
Y_{ln} — mole fraction of air (Natural log mean)

Greek letters

α — thermal diffusivity
α_{ap} — absorber fraction for absorber plate
α_g — absorber fraction for glass cover
ϕ — tilt angle
β — thermal expansion coefficient (1/K)
δ — thickness (m)
e_g — emissivity of glass cover to surrounding
e_p — emissivity of Absorber plate to glass cover
— membrane porosity
λ — latent heat of water (J/kg)
ρ — fluid density of feed solution (kg/m^3)
τ — membrane tortuosity factor
τ_g — glass through fraction
σ — Stefan–Boltzmann constant (kcal $/m^2\ h\ K^4$)
v — kinematics viscosity (m^2/s)
η — thermal efficiency

Subscripts

0 — in glass cover and absorber plate region
1 — In hot stream region
2 — in air gap region
3 — in cold stream region
a — atmosphere
air — air
C — cooling water stream
H — hot saline water stream
i — inlet
m — membrane
o — out
p — plate
solid — solid membrane
T — total
v — vapor
exp. — experimental runs
theo. — theoretical predictions

References

[1] K.W. Lawson, D.R. Lloyd, Membrane distillation, J. Membr. Sci. 124 (1997) 1–25.
[2] A.M. Alklaibi, N. Lior, Membrane-distillation desalination: Status and potential, Desalination 171 (2004) 111–131.
[3] M.S. El-Bourawi, Z. Ding, R. Ma, M. Khayet, A framework for better understanding membrane distillation separation process, J. Membr. Sci. 285 (2006) 4–29.
[4] K.W. Lawson, D.R. Lloyd, Membrane distillation. II. Direct contact MD, J. Membr. Sci. 120 (1996) 123–133.
[5] H.M. Ettouney, H.T. El-Dessouky, R.S. Faibish, P.J. Gowin, Evaluating the economics of desalination, Chem. Eng. Prog. 98 (2002) 32–39.
[6] S. Alobaidani, E. Curcio, F. Macedonio, G. Diprofio, H. Alhinai, E. Drioli, Potential of membrane distillation in seawater desalination: Thermal efficiency, sensitivity study and cost estimation, J. Membr. Sci. 323 (2008) 85–98.
[7] C. Charcosset, A review of membrane processes and renewable energies for desalination, Desalination 245 (2009) 214–231.
[8] F. Banat, N. Jwaied, M. Rommel, J. Koschikowski, M. Wieghaus, Performance evaluation of the "large SMADES" autonomous desalination solar-driven membrane distillation plant in Aqaba, Jordan, Desalination 217 (2007) 17–28.
[9] F. Banat, N. Jwaied, M. Rommel, J. Koschikowski, M. Wieghaus, Desalination by a "compact SMADES" autonomous solar-powered membrane distillation unit, Desalination 217 (2007) 29–37.
[10] G.L. Liu, C. Zhu, C.S. Cheung, C.W. Leung, Theoretical and experimental studies on air gap membrane distillation, Heat Mass Transfer 34 (1998) 329–335.
[11] C.M. Guijt, G.W. Meindersma, T. Reith, A.B. dehaan, Air gap membrane distillation: 1. Modelling and mass transport properties for hollow fibre membranes, Sep. Purif. Technol. 43 (2005) 233–244.
[12] C.M. Guijt, G.W. Meindersma, T. Reith, A.B. Haan, Air gap membrane distillation 2. Model validation and hollow fibre module performance analysis, Sep. Purif. Technol. 43 (2005) 245–255.
[13] A.M. Alklaibi, N. Lior, Transport analysis of air-gap membrane distillation, J. Membr. Sci. 255 (2005) 239–253.

[14] S.A. Kalogirou, Solar thermal collectors and applications, Prog. Energy Combust. Sci. 30 (2004) 231–295.
[15] M. Khayet, Solar desalination by membrane distillation: Dispersion in energy consumption analysis and water production costs (a review), Desalination 308 (2013) 89–101.
[16] C. Stanciu, D. Stanciu, Optimum tilt angle for flat plate collectors all over the World—A declination dependence formula and comparisons of three solar radiation models, Energy Convers. Manage. 81 (2014) 133–143.
[17] J. Phattaranawik, R. Jiraratananon, A.G. Fane, Heat transport and membrane distillation coefficients in direct contact membrane distillation, J. Membr. Sci. 212 (2003) 177–193.
[18] P.S. Ayyaswamy, I. Catton, The boundary-layer regime for natural convection in a differentially heated, tilted rectangular cavity, J. Heat Trans. 95 (1973) 543–545.
[19] J.N. Arnold, I. Catton, D.K. Edwards, Experimental investigation of natural convection in inclined rectangular regions of differing aspect rations, J. Heat Trans. 98 (1976) 189–193.
[20] B. Paláncz, Analysis of solar-dehumidification drying, Int. J. Heat Mass Trans. 27 (1984) 647–655.
[21] K.G.T. Hollands, G.D. Raithby, L. Konicek, T.E. Unny, Free convection heat transfer across inclined air layers, J. Heat Trans. 98 (1975) 189–193.
[22] J.A. Duffie, W.A. Beckman, Solar Engineering of Thermal Processes, third ed., Wiley, New York, NY, 2006.
[23] J.H. Zhang, S. Gray, J.D. Li, Modelling heat and mass transfers in DCMD using compressible membranes, J. Membr. Sci. 387–388 (2012) 7–16.
[24] S.B. Iversen, V.K. Bhatia, K. Dam-Johansen, G. Jonsson, Characterization of microporous membranes for use in membrane contactors, J. Membr. Sci. 130 (1997) 205–217.
[25] R.W. Schofield, A.G. Fane, C.J.D. Fell, Heat and mass transfer in membrane distillation, J. Membr. Sci. 33 (1987) 299–313.
[26] E. Guillén-Burrieza, J. Blanco, G. Zaragoza, D.-C. Alarcón, P. Palenzuela, M. Ibarra, W. Gernjak, Experimental analysis of an air gap membrane distillation solar desalination pilot system, J. Membr. Sci. 379 (2011) 386–396.